

# Two-dimensional Obstructed Atomic Insulators with Fractional Corner Charge in $MA_2Z_4$ Family

Lei Wang,<sup>1,2,\*</sup> Yi Jiang,<sup>3,\*</sup> Jiayi Liu,<sup>1,2</sup> Shuai Zhang,<sup>3,4</sup> Jiangxu Li,<sup>1,2</sup>  
Peitao Liu,<sup>1</sup> Yan Sun,<sup>1</sup> Hongming Weng,<sup>3,4,5</sup> and Xing-Qiu Chen<sup>1,2,†</sup>

<sup>1</sup>Shenyang National Laboratory for Materials Science, Institute of Metal Research,  
Chinese Academy of Science, 110016 Shenyang, Liaoning, People's Republic of China

<sup>2</sup>School of Materials Science and Engineering, University of Science and Technology of China,  
Shenyang 110016, People's Republic of China

<sup>3</sup>Beijing National Laboratory for Condensed Matter Physics,  
and Institute of Physics, Chinese Academy of Sciences, Beijing 100190, China

<sup>4</sup>University of Chinese Academy of Sciences, Beijing 100049, China

<sup>5</sup>Songshan Lake Materials Laboratory, Dongguan, Guangdong 523808, China

(Dated: May 5, 2022)

According to topological quantum chemistry, a class of electronic materials have been called obstructed atomic insulators (OAIs), in which a portion of valence electrons necessarily have their centers located on some empty *Wyckoff* positions without atoms occupation in the lattice. The obstruction of centering these electrons coinciding with their host atoms is nontrivial and results in metallic boundary states when the boundary is properly cut. Here, on basis of first-principles calculations in combination with topological quantum chemistry analysis, we propose two dimensional  $MA_2Z_4$  ( $M = \text{Cr, Mo}$  and  $W$ ;  $A = \text{Si}$  and  $\text{Ge}$ ,  $Z = \text{N, P}$  and  $\text{As}$ ) monolayer family are all OAIs. A typical case is the recently synthesized  $\text{MoSi}_2\text{N}_4$ . Although it is a topological trivial insulator with the occupied electronic states being integer combination of elementary band representations, it has valence electrons centering empty *Wyckoff* positions. It exhibits unique OAI-induced metallic edge states along the  $(1\bar{1}0)$  edge of  $\text{MoSi}_2\text{N}_4$  monolayer and the in-gap corner states at three vertices of certain hexagonal nanodisk samples respecting  $C_3$  rotation symmetry. The readily synthesized  $\text{MoSi}_2\text{N}_4$  is quite stable and has a large bulk band gap of 1.94 eV, which makes the identification of these edge and corner states most possible for experimental clarification.

*Introduction.* –Topological materials including topological insulators and topological semimetals have attracted intensive attentions<sup>1–31</sup>, mainly due to their nontrivial bulk band dispersion and metallic surface (or edge) states. In recent years, the development of topological quantum chemistry (TQC)<sup>32–34</sup> and symmetry indicator<sup>35,36</sup> provides convenient and efficient tools to the high-throughput discoveries of topological quantum materials<sup>37–41</sup>. Within the TQC theory, topological trivial insulators can be defined by band representations (BRs) of valence bands, which are equivalent to a set of exponentially localized Wannier functions<sup>42</sup>. Any BRs can be given by a linear combination of elementary band representations (EBRs), which are induced from irreducible representations at maximal *Wyckoff* positions (WPs)<sup>42–44</sup>. If some of the coefficients of linear combination of elementary band representations (LCEBRs) are rational fractions, the material is a stable topological insulator or topological semimetal. If all the LCEBRs of a material exhibit non-negative integer coefficients, the materials is then a topological trivial insulator<sup>45</sup>.

Recently, a series of unique topologically trivial insulators, dubbed obstructed atomic insulators (OAIs), have been found<sup>45,46</sup>. In difference from the BRs of atomic insulators induced from the atomic orbitals locating at atom-occupied *Wyckoff* positions (AOWPs), the BRs of OAIs are induced from additional atom-unoccupied *Wyckoff* positions (AUWPs). In other words, for atomic insulators electrons fill atomic orbitals at the AOWPs, but for OAIs a portion of electrons have to occupy those at the AUWPs. Note that in any periodic lattice of solid materials there are many so-called AUWPs, which can be easily identified via the international tables for crystallography. Nevertheless, not all AUWPs are

necessary for OAIs, while only those electron-filled AUWPs are necessary for OAIs. Such electron-filled AUWPs for OAIs are also named as obstructed Wannier charge centers (OWCCs)<sup>45</sup>. Importantly, when the cleavage termination cuts through those electron-filled AUWPs (namely, OWCCs) in an OAI, the metallic surface states will emerge. This crucial feature makes OAIs be potential candidates for superconductivity and catalysis<sup>46–50</sup>. To date, OAIs including 3,383 paramagnetic and 30 magnetic materials are reported in three-dimensional (3D) materials<sup>45,46</sup>. However, 2D OAIs, which could be used in low dimensional devices<sup>51,52</sup>, have not been systematically investigated.

Recently, 2D monolayer  $MA_2Z_4$  family<sup>53,54</sup> with septuple-atomic-layer lattices have been experimentally or theoretically reported. This  $MA_2Z_4$  family crystallizes in five different crystalline phases, including 72 theoretically suggested stable materials<sup>54</sup>. By inspecting the electronic structure of theoretically predicted stable monolayer  $\alpha_1\text{-WSn}_2\text{N}_4$  semiconductor with an indirect band gap of 0.18 eV, we found that it possesses the typical inverted energy band between  $W-d_{z^2}$  and  $N-p_z$  orbitals at the centered  $\Gamma$  point of the Brillouin Zone (BZ) around the band gap (Appendix Fig. A1). Although the band inversion typically signals to have nontrivial topological nature, both its topological indicator and mirror chern number equal to zero, indicating a topological trivial insulator. Furthermore, by deriving its electronic band structure of the edge boundary, metallic edge states nevertheless occur, which is very similar to the metallic surface states of 3D OAIs<sup>45,46</sup>. Interestingly, we further revealed that in total 16 monolayer  $MA_2Z_4$  semiconductors with 34 valence electrons (VEC) including experimentally synthesized  $\alpha_1\text{-MoSi}_2\text{N}_4$  exhibit sim-

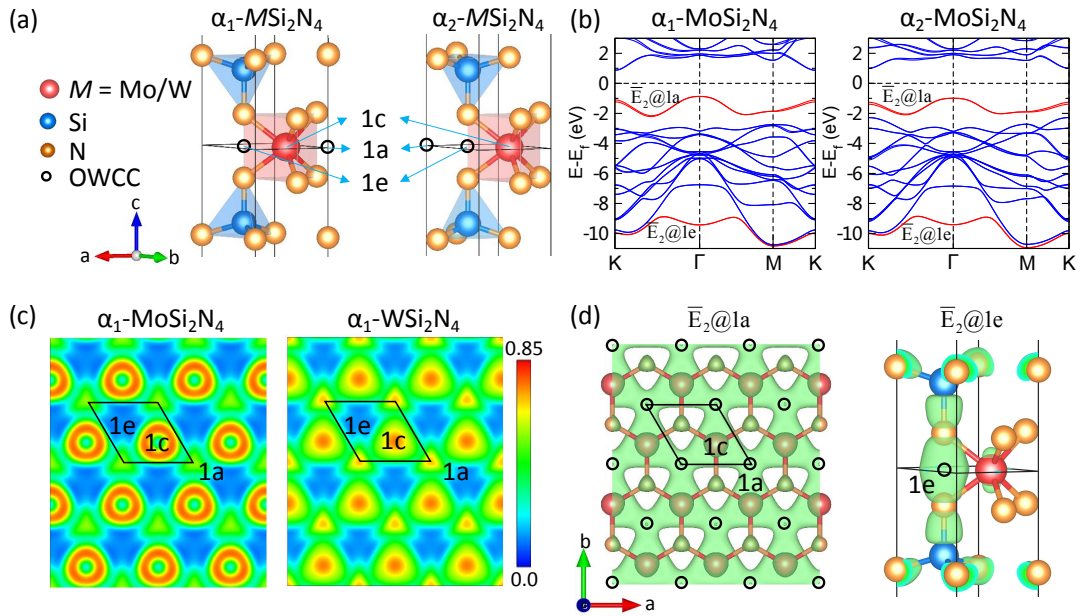


FIG. 1. (Color online) Lattice and electronic structures of  $MSi_2N_4$  monolayer ( $M = \text{Mo}, \text{W}$ ). (a) Lattice structures of  $\alpha_1$ - and  $\alpha_2$ - $MSi_2N_4$  monolayer, where the black circle denotes the obstructed wannier charge center (OWCC). (b) The electronic band structures of  $\alpha_1$ - and  $\alpha_2$ - $MoSi_2N_4$  monolayer with the inclusion of spin-orbit coupling, where the red bands correspond to the band representation of  $\bar{E}_2@1a$  and  $\bar{E}_2@1e$ . (c) The electron localization functions (ELF) of  $\alpha_1$ - $MoSi_2N_4$  and  $\alpha_1$ - $WSi_2N_4$  monolayer.  $1a$ ,  $1c$ , and  $1e$  are *Wyckoff* positions, and the localized charges occupy at the  $1a$  and  $1c$  *Wyckoff* positions. The solid lines denote the primitive cell of  $\alpha_1$ - $MSi_2N_4$  monolayer materials. (d) The charges distribution of the band representation  $\bar{E}_2@1a$  and  $\bar{E}_2@1e$  of  $\alpha_1$ - $MoSi_2N_4$ . The green hook face is the isosurface with value of  $0.008 \text{ e}/\text{\AA}^3$  and the black circles denote the OWCCs at both  $1a$  and  $1e$ . In the left panel of (d), to show  $1a$  position clearly, the top and bottom Si-N layers of  $\alpha_1$ - $MoSi_2N_4$  monolayer are removed.

ilar electronic band features to  $\alpha_1$ - $WSn_2N_4$  and they all are topological trivial insulators. Their special electronic structures make us think over whether these monolayer  $MA_2Z_4$  semiconductors are 2D OAI. If yes, any novel properties will emerge in these 2D OAI family?

With this motivation, by means of first-principles calculations in combination with TQC analysis, we report 16 monolayer 34-VEC  $MA_2Z_4$  semiconductors as 2D OAI. By taking the experimentally synthesized  $MoSi_2N_4$  semiconductor as a typical example, we identify the occurrence of the localized charge at the AUWPs as the crucial fingerprint of OAIs. Additionally, the metallic edge states appear in the band gap along the  $(1\bar{1}0)$  direction on the boundary of  $MoSi_2N_4$  monolayer at which cleavage terminations exactly cut through OWCCs. Interestingly, in-gap corner states found in second-order topological insulators also occur in the  $C_3$ -symmetric hexagonal nanodisk of  $MoSi_2N_4$ .

*Lattice structure of  $MoSi_2N_4$  monolayer.* — The experimentally synthesized  $\alpha_1$ - $MoSi_2N_4$ <sup>53</sup> with 34 VEC belongs to  $MA_2Z_4$  family<sup>54</sup>. In our theoretical predictions<sup>54</sup>, there are 15 monolayer 34-VEC  $MA_2Z_4$  semiconductors, which mainly crystallize in two classes of lattice structures,  $\alpha_1$ - and  $\alpha_2$ - $MA_2Z_4$ . For  $MoSi_2N_4$ , the formation energy of  $\alpha_1$ - $MoSi_2N_4$  is 24 meV/atom lower than that of  $\alpha_2$ - $MoSi_2N_4$ . Similarly,  $\alpha_1$  phase of  $WSn_2N_4$  is energetically more stable by 1.3 meV/atom than its  $\alpha_2$  phase. Both  $\alpha_1$ - and  $\alpha_2$ - $MoSi_2N_4$

have the hexagonal lattices with the atomic sequence of N-Si-N-Mo-N-Si-N (the space group of  $P\bar{6}m2$  (No. 187)<sup>2</sup>), as shown in Fig. 1(a). This septuple-atom-layer can be viewed by inserting 2H- $MoS_2$ -type  $MoN_2$  into  $\alpha$ -InSe-type SiN. In  $\alpha_1$ - $MoSi_2N_4$  there are two different nitrogen WPs of  $2g$  ( $0, 0, \pm z$ ) and  $2i$  ( $2/3, 1/3, \pm z$ ), whereas for  $\alpha_2$ - $MoSi_2N_4$  two different nitrogen WPs of  $2h$  ( $1/3, 2/3, \pm z$ ) and  $2i$  ( $2/3, 1/3, \pm z$ ). Thus, here we denote three different nitrogen WPs as  $N_g$ ,  $N_i$ , and  $N_h$  for sake of convenient discussion below. As illustrated in Fig. 1(a), both  $N_g$  for  $\alpha_1$ - $MoSi_2N_4$  and  $N_h$  for  $\alpha_2$ - $MoSi_2N_4$  locate at the top or the bottom of the monolayer  $MoSi_2N_4$ , but  $N_i$  atoms sit in the layer between Si of  $2i$  ( $2/3, 1/3, \pm z$ ) and Mo of  $1c$  ( $1/3, 2/3, 0$ ). Thus, nitrogen atoms form two basic local structures, a tetrahedron consisting of three  $N_g$  (or  $N_h$ ) atoms and one  $N_i$  atom, and a triangular prism composed of six  $N_i$  atoms. Si and Mo atoms sit at the centering positions of the tetrahedron and the prism, respectively. It needs to be emphasized that  $N_i$  and Si atoms have the same *Wyckoff* notations of  $2i$  ( $2/3, 1/3, \pm z$ ) but with different  $z$  values.

*OAI identification of  $MoSi_2N_4$  monolayer.* —  $\alpha_1$ - $MoSi_2N_4$  is an indirect semiconductor with an experimental band gap of 1.94 eV, comparable to the DFT-derived gap of 1.74 eV (PBE) and 2.30 eV (HSE06)<sup>54</sup>. It is also a topologically trivial insulator, according to topological analysis using mirror chern number. Conceptually, the occupied electronic bands

TABLE I. All possible decompositions of the BRs of  $\alpha_1$ -MoSi<sub>2</sub>N<sub>4</sub> and  $\alpha_2$ -MoSi<sub>2</sub>N<sub>4</sub> into linear combinations of the EBRs in the double space group P6m2 (No. 187). The first row gives the possible EBRs induced from different orbitals at the *Wyckoff* positions 1*a*, 1*c*, and 1*e*; the numbers below are the multiplicities of each EBR in the corresponding decomposition. Note that only a portion of LCEBRs are listed here and the complete LCEBRs are given in the Appendix Table A1 and Table A2.

Compounds	$\bar{E}_1@1a$	$\bar{E}_2@1a$	$\bar{E}_3@1a$	$\bar{E}_1@1c$	$\bar{E}_2@1c$	$\bar{E}_3@1c$	$\bar{E}_1@1e$	$\bar{E}_2@1e$	$\bar{E}_3@1e$
$\alpha_1$ -MoSi <sub>2</sub> N <sub>4</sub>	6	7	5	1	0	0	1	1	0
	5	6	4	2	1	1	1	1	0
	4	5	3	3	2	2	1	1	0
	3	4	2	4	3	3	1	1	0
	2	3	1	5	4	4	1	1	0
	1	2	0	6	5	5	1	1	0
$\alpha_2$ -MoSi <sub>2</sub> N <sub>4</sub>	5	6	5	2	1	0	1	1	0
	4	5	4	3	2	1	1	1	0
	3	4	3	4	3	2	1	1	0
	2	3	2	5	4	3	1	1	0
	1	2	1	6	5	4	1	1	0
	0	1	0	7	6	5	1	1	0

of 3D topological trivial insulator can be expressed by a non-negative integer linear combination of EBRs using the TQC theory<sup>32–34</sup>. Since MoSi<sub>2</sub>N<sub>4</sub> monolayer is a 2D material, only the band representations (BRs) of high symmetry points  $\Gamma$ , M and K at  $k_z=0$  plane are considered. And since the EBRs of *Wyckoff* positions 2*g*, 2*h* and 2*i* can be obtained by the combinations of EBRs of *Wyckoff* positions 1*a*, 1*c*, and 1*e*, the maximum *Wyckoff* positions 1*a*, 1*c*, and 1*e* are chosen to perform the EBRs decomposition. Therefore, the LCEBRs of the occupied electronic bands of  $\alpha_1$ - and  $\alpha_2$ -MoSi<sub>2</sub>N<sub>4</sub> have been derived in Table I. Note that we only listed a portion of LCEBRs, and the complete LCEBRs of  $\alpha_1$ - and  $\alpha_2$ -MoSi<sub>2</sub>N<sub>4</sub> can be found in Appendix Table A1 and Table A2, respectively. Interestingly, for  $\alpha_1$ -MoSi<sub>2</sub>N<sub>4</sub>, the results of all the LCEBRs show that there are six EBRs ( $\bar{E}_1@1a$ ,  $\bar{E}_2@1a$ ,  $\bar{E}_1@1c$ ,  $\bar{E}_2@1c$ ,  $\bar{E}_1@1e$  and  $\bar{E}_2@1e$ ) with the non-zero integer combination. This fact means these six EBRs can not be decomposed and they have to be linked to electron-filled *Wyckoff* positions of 1*a*, 1*c*, and 1*e*. The 1*c* site is occupied by Mo atom whereas the 1*a* and 1*e* sites are *null* without any atomic occupation. In terms of the OAI definition<sup>45,46</sup>,  $\alpha_1$ -MoSi<sub>2</sub>N<sub>4</sub> is an OAI and the 1*a* and 1*e* sites are the OWCC. Similarly, the non-zero integer of LCEBR of the 1*a* and 1*e* AUWPs indicates that  $\alpha_2$ -MoSi<sub>2</sub>N<sub>4</sub> is also an OAI, and the 1*a* and 1*e* AUWPs are the OWCC.

For the OAI feature, the most key point is to check whether the AUWPs have the localized charges (namely, electron filling). To elucidate the real-space charge localizations of MoSi<sub>2</sub>N<sub>4</sub> we have thus visualized the electron localization function (ELF) (Fig. 1(c)) on the centering Mo-atom layer in which four indecomposable EBRs correspond to both 1*a* (*null*) and 1*c* (Mo) AUWP. It can be seen that the charges obviously localize at the 1*c* Mo site and the *null* 1*a* AUWP. The feature is more apparent in  $\alpha_1$ -WSi<sub>2</sub>N<sub>4</sub> and  $\alpha_2$ -MoSi<sub>2</sub>N<sub>4</sub> (see Appendix Fig. A2). We find that the localized charges at the 1*c* AOWP are mainly contributed by Mo atoms, whereas the ones at the *null* 1*a* AUWP originate from the orbital hybridizations between Mo and N<sub>*i*</sub> atoms, which is in good agreement

with obstructed atomic limit for SSH model with *sp* orbital hybridization<sup>32</sup>. Furthermore, in Fig. 1(d) we plot the partial charge densities of the two indecomposable EBRs responsible for the isolated electronic bands marked by  $\bar{E}_2@1a$  and  $\bar{E}_2@1e$  in Fig. 1(b), evidencing the distribution of charges at both the 1*a* and 1*e* AUWPs.

Following the similar analysis, we have checked another 15 MA<sub>2</sub>Z<sub>4</sub> monolayer semiconductors with 34 valence electrons predicted in our previous work<sup>54</sup>. The results demonstrate that all of them are typical OAIs, as summarized in Appendix Table A3.

*Obstructed metallic edge states and in-gap corner states.* — Physically, topological nontrivial materials with *d*-1 dimensional boundary states are defined as first-order topological materials (where *d* is the dimension of topological materials). The ones with *d*-*n* (*n* > 1) dimensional boundary states are the *n*th order topological materials. Interestingly, In similarity with 3D topological insulators, for a 3D OAI the *d*-1 dimensional metallic surface states occur on the 2D surface with the cleavage terminations exactly cutting through an OWCC<sup>45,46</sup>. Hence, it is desirable to examine to see whether or not the metallic edge states of the 1D boundary occur for the 2D OAI of monolayer MoSi<sub>2</sub>N<sub>4</sub>.

Note that because for  $\alpha_1$ -MoSi<sub>2</sub>N<sub>4</sub> its two N<sub>*g*</sub> and two N<sub>*i*</sub> atoms are exactly above its OWCC-type 1*a* (0, 0, 0) and 1*e* (2/3, 1/3, 0) AUWPs, it is hard to cut an edge that only contains the OWCC but without containing the N atoms. However, this difficulty does not occur in its  $\alpha_2$  phase of OAI, since no atoms are exactly above its OWCC-type 1*a* AUWP (see Fig. 1(a) and Table I). On basis of Wannier-based Hamiltonian of  $\alpha_2$ -MoSi<sub>2</sub>N<sub>4</sub>, we derived the electronic band structures of the edge boundary along (1 $\bar{1}$ 0) direction, which only cuts through the OWCC-type 1*a* (0, 0, 0) AUWP (Fig. 2(a-c)). Notably, the apparent obstructed metallic edge states (OESs) occur between the conduction bands (CB) and valence bands (VB) of  $\alpha_2$ -MoSi<sub>2</sub>N<sub>4</sub> monolayer. This phenomenon agrees well with the observations in 3D OAIs<sup>45,46</sup>. By calculating the charge distribution of the OESs at the Fermi level within a

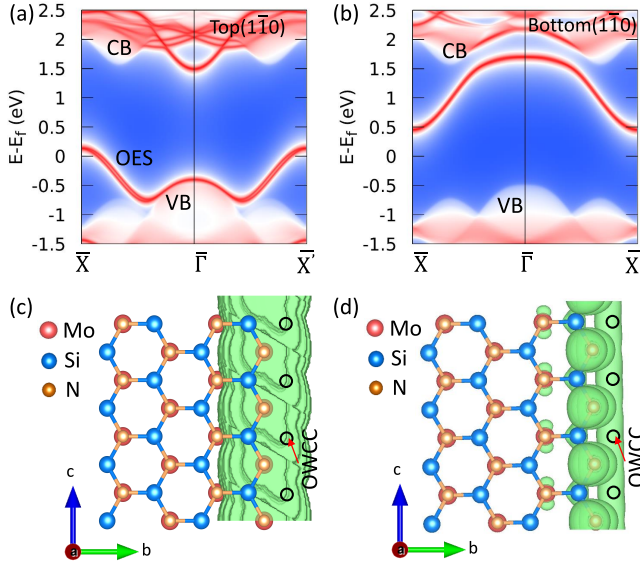


FIG. 2. (Color online) Obstructed metallic edge states of  $\alpha_2$ - $\text{MoSi}_2\text{N}_4$  monolayer. (a-b) The projected edge states along the  $(1\bar{1}0)$  direction of the boundary with cutting through the OWCC at  $1a$  site. CB and VB are the conduction bands and valence bands. OES is the obstructed metallic edge states. (c) Charge distributions of metallic OES at Fermi level shown in (a) derived by Wannier-based Hamiltonian of  $\alpha_2$ - $\text{MoSi}_2\text{N}_4$  nanoribbon. (d) Charge distributions of metallic OES at Fermi level shown in (a) derived by first-principles calculations of  $\alpha_2$ - $\text{MoSi}_2\text{N}_4$  nanoribbon. The black circle marked by red arrow are OWCC. Green hook face is the isosurface of the charge of OES with a value of  $0.002 e/\text{\AA}^3$ .

nanowire model with a width of 20 unit cells, the charges localize around the OWCC-type  $1a$  AUWP and the decay of the OESs only has a depth of about 0.4 nm, as seen in Fig. 2(c). Such result is also verified by the first-principles calculations, in Fig. 2(d).

Next we turn to checking whether or not the 2D OAI of monolayer  $\text{MoSi}_2\text{N}_4$  has the  $d-2$  dimensional (namely zero-dimensional (0D)) in-gap corner states. We derived the electronic structures of the 0D nanodisk modeling of  $\alpha_1$ - $\text{MoSi}_2\text{N}_4$ . By analyzing its structural details (see Appendix Fig. A3, Fig. A4, and Table A4), we constructed a  $C_3$ -symmetric triangle and hexagonal nanodisk with the armchair edge to keep the electrically neutral stoichiometric ratio of 1:2:4 over Mo:Si:N. Since monolayer  $\text{MoSi}_2\text{N}_4$  holds three types of maximum *Wyckoff* positions, there are three possible geometries for both triangle and hexagonal nanodisks by varying the type of atom at center site. No matter which type of atom sits at the center of the  $C_3$ -symmetric triangle or hexagonal nanodisk, their stoichiometric ratio is always remained by removing the center atoms (see Appendix Table A4).

To argue whether the monolayer  $\text{MoSi}_2\text{N}_4$  holds the in-gap corner states, one has to see the so-called gapped edge states on the boundaries and the in-gap corner states siting the vertexes of the  $C_3$ -symmetric triangle or hexagonal nanodisk. However, depending on the *filling anomaly* at the center

site, the in-gap corner states certainly occur in  $C_3$ -symmetric triangle and hexagonal nanodisk.

Recently, a general formula to calculate the corner charges of the  $C_n$  symmetry nanodisk was developed<sup>55-57</sup>, as follows,

$$Q_{\text{corner}} = Q_{c-X}^{(n)} \equiv \frac{(n_X^{(\text{ion})} - n_X^{(e)}) |e|}{n} \pmod{|e|}, \quad (1)$$

where  $Q_{c-X}^{(n)}$  means the corner charge when the center of the crystal locates at the  $X$  site,  $n$  is the fold of rotation axis.  $n_X^{(\text{ion})} |e|$  and  $n_X^{(e)}$  are the ionic charges and the number of electronic Wannier functions at the  $X$  site, respectively. Applying Eq. 1 to monolayer  $\text{MoSi}_2\text{N}_4$ , we obtained the corner charge of the  $C_3$ -symmetric triangle or hexagonal nanodisk of  $Q_{1a}^{(n)} = 1/3 |e|$ ,  $Q_{1e}^{(n)} = 2/3 |e|$  and  $Q_{1c}^{(n)} = 0 |e|$ . Here, the  $1a$ ,  $1e$  and  $1c$  sites are responsible for the N, Si and Mo atoms at the center of the  $C_3$ -symmetric crystals. Furthermore, we derived the energy spectra and charge distributions of our constructed triangle or hexagonal nanodisk. Note that the energy spectra and charge distribution of the N-centered hexagonal nanodisk are further compiled in Fig. 3(a, d), while the others are given in Appendix Fig. A5. It can be seen that three corner states at the N atoms meeting the  $C_3$  rotational symmetry are in-gap and nearly zero-energy, labeling Nos. 718, 719 and 720. The other three corners without any charge distribution can be actually viewed as charge neutral "edges". The states of Nos. 718 and 719 are occupied and the No. 720 states are unoccupied. Because this system is spinless and the number of electrons of this system is 1438, we need to add two or subtract four electrons to make this system fully occupied or fully empty so that the system is gapped. The added two or subtracted four electrons correspond to  $-2/3 |e|$  and  $4/3 |e|$  corner charge at its each  $C_3$ -symmetry corner. This result is equivalent to the calculated  $1/3 |e|$  through Eq. 1. We note that the same conditions exist in the corner charge calculations of both Si-centered and Mo-centered hexagonal nanodisks. In Si-centered hexagonal nanodisk, three corner states are separated by one edge state (see Figs. 3(b, e) and Appendix Fig. A6). The corner state below edge state can be pushed into the gap of edge via an appropriate edge potential<sup>32</sup>. In Mo-centered hexagonal nanodisk, the states near the Fermi level are distributed not only at three corners in similarity to those of N-centered hexagonal nanodisk, but also at three charge neutral "edges". Therefore, no corner states occur in their energy level near the Fermi level, which reflects well the zero corner charge of the Mo-centered hexagonal nanodisk (see Figs. 3(c, f) and Appendix Fig. A7).

**Conclusions.** — To summarize, we have identified the 16  $\text{MA}_2\text{Z}_4$  monolayer family materials with 34 valence electrons as 2D obstructed atomic insulators. They are featured by the occurrence of half-filled obstructed metallic edge states in 1D nanowires and in-gap corner states in 0D  $C_3$ -symmetric hexagonal nanodisks. Moreover, the 2H- $\text{MoS}_2$  monolayer and  $\alpha$ - $\text{InSe}$  monolayer, the two basic constituent units for the  $\text{MA}_2\text{Z}_4$  monolayer family, are also identified as obstructed atomic insulators. Our work proposes a promising realization of 2D obstructed atomic insulators without inversion symmetry and provides a new platform to explore exotic phases of condensed matter and their associated novel properties.



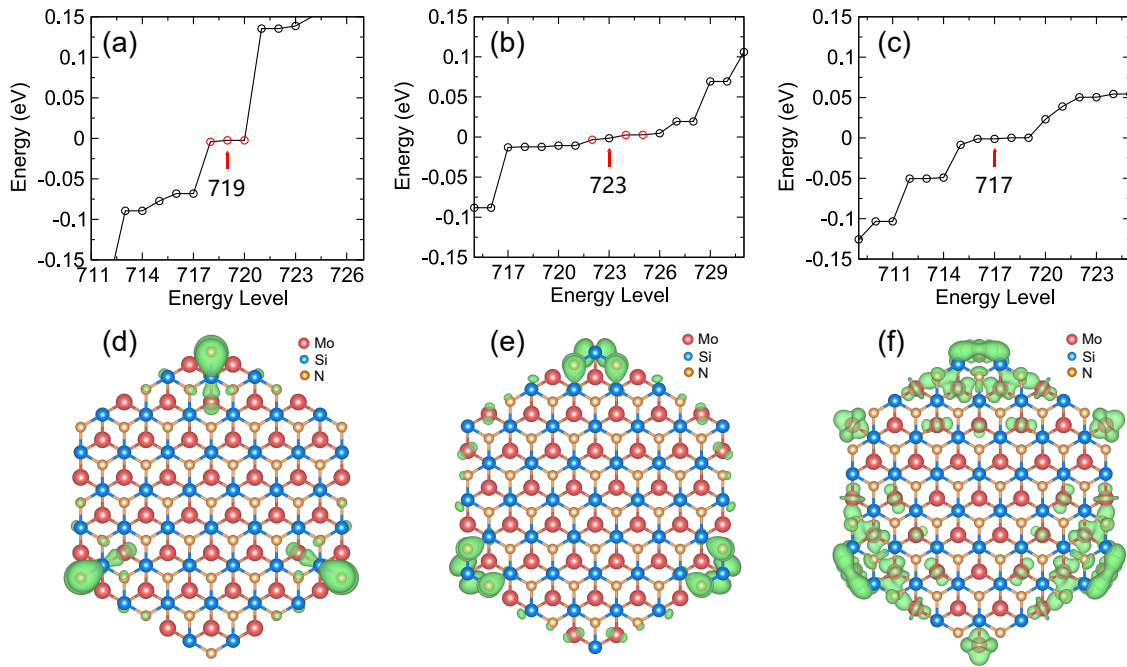


FIG. 3. (Color online) (a-c) Energy spectra of  $C_3$ -symmetric hexagonal-shaped nanodisk of  $\alpha_1$ - $\text{MoSi}_2\text{N}_4$  with the N, Si, and Mo atom in the center, where the occupied energy level is marked by the red arrow and red circles represent corner states. (d-f) The charge distributions of the 718, 722, and 716 energy levels appearing in (a)-(c), respectively.

*Acknowledgments.* — Work was supported by the National Science Fund for Distinguished Young Scholars (grant number 51725103), the National Natural Science Foundation (Grant No. 11925408, 11921004 and 12188101), the Ministry of Science and Technology of China (Grant No. 2018YFA0305700), the Chinese Academy of Sciences (Grant

No. XDB33000000), the K. C. Wong Education Foundation (GJTD-2018-01), and the Informatization Plan of Chinese Academy of Sciences (Grant No. CAS-WX2021SF-0102). All calculations have been performed on the high-performance computational cluster in the Shenyang National University Science and Technology Park.

\* These authors contributed equally to this work

† xingqiu.chen@imr.ac.cn

<sup>1</sup> M. Z. Hasan and C. L. Kane, *Rev. Mod. Phys.* **82**, 3045 (2010).

<sup>2</sup> X.-L. Qi and S.-C. Zhang, *Topological Insulators and Superconductors*, *Rev. Mod. Phys.* **83**, 1057 (2011).

<sup>3</sup> B. A. Bernevig, T. L. Hughes, and S.-C. Zhang, *Science* **314**, 1757 (2006).

<sup>4</sup> M. König, S. Wiedmann, C. Brüne, A. Roth, H. Buhmann, L. W. Molenkamp, X.-L. Qi, and S.-C. Zhang, *Science* **318**, 766 (2007).

<sup>5</sup> D. Hsieh, D. Qian, L. Wray, Y. Xia, Y. S. Hor, R. J. Cava, and M. Z. Hasan, *Nature* **452**, 7190 (2008).

<sup>6</sup> D. Hsieh, Y. Xia, D. Qian, L. Wray, J. H. Dil, F. Meier, J. Osterwalder, L. Patthey, J. G. Checkelsky, N. P. Ong, A. V. Fedorov, H. Lin, A. Bansil, D. Grauer, Y. S. Hor, R. J. Cava, and M. Z. Hasan, *Nature* **460**, 1101 (2009).

<sup>7</sup> H. Zhang, C.-X. Liu, X.-L. Qi, X. Dai, Z. Fang, and S.-C. Zhang, *Nature Physics* **5**, 438 (2009).

<sup>8</sup> C.-C. Liu, W. Feng, and Y. Yao, *Phys. Rev. Lett.* **107**, 076802 (2011).

<sup>9</sup> L. Fu, *Phys. Rev. Lett.* **106**, 106802 (2011).

<sup>10</sup> T. H. Hsieh, H. Lin, J. Liu, W. Duan, A. Bansil, and L. Fu, *Nature*

*Communications* **3**, 1 (2012).

<sup>11</sup> Z. Wang, Y. Sun, X.-Q. Chen, C. Franchini, G. Xu, H. Weng, X. Dai, and Z. Fang, *Phys. Rev. B* **85**, 195320 (2012).

<sup>12</sup> Z. Wang, H. Weng, Q. Wu, X. Dai, and Z. Fang, *Phys. Rev. B* **88**, 125427 (2013).

<sup>13</sup> H. Weng, C. Fang, Z. Fang, B. A. Bernevig, and X. Dai, *Phys. Rev. X* **5**, 011029 (2015).

<sup>14</sup> R. Li, H. Ma, X. Cheng, S. Wang, D. Li, Z. Zhang, Y. Li, and X.-Q. Chen, *Phys. Rev. Lett.* **117**, 096401 (2016).

<sup>15</sup> H. Xiang, B. Xu, J. Liu, Y. Xia, H. Lu, J. Yin, and Z. Liu, *AIP Advances* **6**, 095005 (2016).

<sup>16</sup> N. Morali, R. Batabyal, P. K. Nag, E. Liu, Q. Xu, Y. Sun, B. Yan, C. Felser, N. Avraham, and H. Beidenkopf, *Science* **365**, 1286 (2019).

<sup>17</sup> S.-C. Zhu, L. Wang, J.-Y. Qu, J.-J. Wang, T. Frolov, X.-Q. Chen, and Q. Zhu, *Phys. Rev. Materials* **3**, 024205 (2019).

<sup>18</sup> Z. Song, Z. Wang, W. Shi, G. Li, C. Fang, and B. A. Bernevig, *Phys. Rev. Lett.* **123**, 036401 (2019).

<sup>19</sup> L. Wang, M. Liu, J. Li, R. Li, H. Ma, and X.-Q. Chen, *Phys. Rev. B* **104**, 195123 (2021).

<sup>20</sup> J. Gao, Y. Qian, S. Nie, Z. Fang, H. Weng, and Z. Wang, *Science*

- Bulletin **66**, 667 (2021).
- 21 F. Schindler, A. M. Cook, M. G. Vergniory, Z. Wang, S. S. P. Parkin, B. A. Bernevig, and T. Neupert, *Science Advances* **4**, eaat0346 (2018).
  - 22 M. Ezawa, *Phys. Rev. B* **98**, 045125 (2018).
  - 23 F. Schindler, Z. Wang, M. G. Vergniory, A. M. Cook, A. Murani, S. Sengupta, A. Y. Kasumov, R. Deblock, S. Jeon, I. Drozdov, H. Bouchiat, S. Guéron, A. Yazdani, B. A. Bernevig, and T. Neupert, *Nature Physics* **14**, 918-924 (2018).
  - 24 C. Yue, Y. Xu, Z. Song, H. Weng, Y.-M. Lu, C. Fang, and X. Dai, *Nature Physics* **15**, 577-581 (2019).
  - 25 Y. Xu, Z. Song, Z. Wang, H. Weng, and X. Dai, *Phys. Rev. Lett.* **122**, 256402 (2019).
  - 26 Z. Wang, B. J. Wieder, J. Li, B. Yan, and B. A. Bernevig, *Phys. Rev. Lett.* **123**, 186401 (2019).
  - 27 X.-L. Sheng, C. Chen, H. Liu, Z. Chen, Z.-M. Yu, Y. X. Zhao, and S. A. Yang, *Phys. Rev. Lett.* **123**, 256402 (2019).
  - 28 B. Liu, G. Zhao, Z. Liu, and Z. F. Wang, *Nano Lett.* **19**, 6492 (2019).
  - 29 H. Mu, B. Liu, T. Hu, and Z. Wang, *Nano Lett.* **22**, 1122-1128 (2022).
  - 30 C. Chen, Z. Song, J.-Z. Zhao, Z. Chen, Z.-M. Yu, X.-L. Sheng, and S. A. Yang, *Phys. Rev. Lett.* **125**, 056402 (2020).
  - 31 S. Qian, C.-C. Liu, and Y. Yao, *Phys. Rev. B* **104**, 245427 (2021).
  - 32 Barry Bradlyn, L. Elcoro, Jennifer Cano, M. G. Vergniory, Zhijun Wang, C. Felser, M. I. Aroyo, and B. Andrei Bernevig, *Nature* **547**, 298-305 (2017).
  - 33 Luis Elcoro, Benjamin J. Wieder, Zhida Song, Yuanfeng Xu, Barry Bradlyn, and B. Andrei Bernevig, *Nat. Commun.* **12**, 5965 (2021).
  - 34 Bingrui Peng, Yi Jiang, Zhong Fang, Hongming Weng, and Chen Fang, *arXiv preprint arXiv:2102.12645* (2021).
  - 35 Hoi Chun Po, Ashvin Vishwanath, and Haruki Watanabe, *Nat. Commun.* **8**, 50 (2017).
  - 36 Haruki Watanabe, Hoi Chun Po, and Ashvin Vishwanath, *Science Advances* **4**, eaat8685 (2018).
  - 37 M. G. Vergniory, L. Elcoro, Claudia Felser, Nicolas Regnault, B. Andrei Bernevig, and Zhijun Wang, *Nature* **566**, 480-485 (2019).
  - 38 Tiantian Zhang, Yi Jiang, Zhida Song, He Huang, Yuqing He, Zhong Fang, Hongming Weng, and Chen Fang, *Nature* **566**, 475-479 (2019).
  - 39 Feng Tang, Hoi Chun Po, Ashvin Vishwanath, and Xiangang Wan, *Nature* **566**, 486-489 (2019).
  - 40 Yuanfeng Xu, Luis Elcoro, Zhi-Da Song, Benjamin J. Wieder, M. G. Vergniory, Nicolas Regnault, Yulin Chen, Claudia Felser, and B. Andrei Bernevig, *Nature* **586**, 702-707 (2020).
  - 41 Maia G. Vergniory, Benjamin J. Wieder, Luis Elcoro, Stuart S. P. Parkin, Claudia Felser, B. Andrei Bernevig, and Nicolas Regnault, *arXiv:2105.09954* (2021).
  - 42 J. Cano, B. Bradlyn, Z. Wang, L. Elcoro, M. G. Vergniory, C. Felser, M. I. Aroyo, and B. A. Bernevig, *Phys. Rev. B* **97**, 035139 (2018).
  - 43 L. Elcoro, B. Bradlyn, Z. Wang, M. G. Vergniory, J. Cano, C. Felser, B. A. Bernevig, D. Orobengoa, G. de la Flor, and M. I. Aroyo, *J Appl Cryst* **50**, 5 (2017).
  - 44 M. G. Vergniory, L. Elcoro, Z. Wang, J. Cano, C. Felser, M. I. Aroyo, B. A. Bernevig, and B. Bradlyn, *Phys. Rev. E* **96**, 023310 (2017).
  - 45 Y. Xu, L. Elcoro, Z.-D. Song, M. G. Vergniory, C. Felser, S. S. P. Parkin, N. Regnault, J. L. Mañes, and B. A. Bernevig, *arXiv:2106.10276* (2021).
  - 46 Y. Xu, L. Elcoro, G. Li, Z.-D. Song, N. Regnault, Q. Yang, Y. Sun, S. Parkin, C. Felser, and B. A. Bernevig, *arXiv:2111.02433* (2021).
  - 47 J. Gao, Y. Qian, H. Jia, Z. Guo, Z. Fang, M. Liu, H. Weng, and Z. Wang, *arXiv:2106.08035* (2021).
  - 48 S. Nie, Y. Qian, J. Gao, Z. Fang, H. Weng, and Z. Wang, *Phys. Rev. B* **103**, 205133 (2021).
  - 49 R. Banerjee, S. Mandal, and T. C. H. Liew, *Phys. Rev. Lett.* **124**, 063901 (2020).
  - 50 H. Wu, Y. Wang, Y. Xu, P. K. Sivakumar, C. Pasco, U. Filippozzi, S. S. P. Parkin, Y.-J. Zeng, T. McQueen, and M. N. Ali, *Nature* **604**, 7907 (2022).
  - 51 E. Lee, R. Kim, J. Ahn, and B.-J. Yang, *Npj Quantum Mater.* **5**, 1 (2020).
  - 52 M. Pan, D. Li, J. Fan, and H. Huang, *Npj Comput Mater* **8**, 1 (2022).
  - 53 Y.-L. Hong, Z. Liu, L. Wang, T. Zhou, W. Ma, C. Xu, S. Feng, L. Chen, M.-L. Chen, D.-M. Sun, X.-Q. Chen, H.-M. Cheng, and W. Ren, *Science* **369**, 670 (2020).
  - 54 L. Wang, Y. Shi, M. Liu, A. Zhang, Y.-L. Hong, R. Li, Q. Gao, M. Chen, W. Ren, H.-M. Cheng, Y. Li, and X.-Q. Chen, *Nat. Commun.* **12**, 2361 (2021).
  - 55 R. Takahashi, T. Zhang, and S. Murakami, *Phys. Rev. B* **103**, 205123 (2021).
  - 56 W. A. Benalcazar, T. Li, and T. L. Hughes, *Phys. Rev. B* **99**, 245151 (2019).
  - 57 F. Schindler, M. Brzezińska, W. A. Benalcazar, M. Iraola, A. Bouhon, S. S. Tsirkin, M. G. Vergniory, and T. Neupert, *Phys. Rev. Research* **1**, 033074 (2019).
  - 58 G. Kresse and J. Furthmüller, *Physical Review B* **54**, 11169 (1996).
  - 59 G. Kresse and D. Joubert, *Physical Review B* **59**, 1758 (1999).
  - 60 A. Togo and I. Tanaka, *Scripta Materialia* **108**, 1 (2015).
  - 61 M. P. L. Sancho, J. M. L. Sancho, and J. Rubio, *J. Phys. F* **15**, 851 (1985).
  - 62 A. A. Mostofi, J. R. Yates, G. Pizzi, Y.-S. Lee, I. Souza, D. Vanderbilt, and N. Marzari, *Computer Physics Communications* **185**, 2309 (2014).

## Appendix A: Computational methods

Vienna ab *initio* simulation package (VASP)<sup>58,59</sup> with exchange-correlation potential of Perdew-Burke-Ernzerhof (PBE) and projector augmented wave (PAW) method was used to perform first-principles calculations. 20 Å vacuum was set to exclude the interactions between the layers with periodic images. 500 eV cutoff energy and  $15 \times 15 \times 1$   $k$ -mesh in  $\Gamma$ -centered Monkhorst-Pack scheme were chosen in self-consistent calculation process. The structure was optimized until the force and energy less than  $10^{-3}$  eV/Å and  $10^{-6}$  eV/Å, respectively. All the  $C_3$ -symmetric nanodisks were calculated by only  $\Gamma$  points. In addition, combating with Wannier90<sup>62</sup> code, density functional theory (DFT)-derived Wannier functions (WFs) was constructed. And the Hamiltonians for each compounds were derived. Iterative Green functions method<sup>61</sup> was applied to calculate the semi-infinite spectral function.

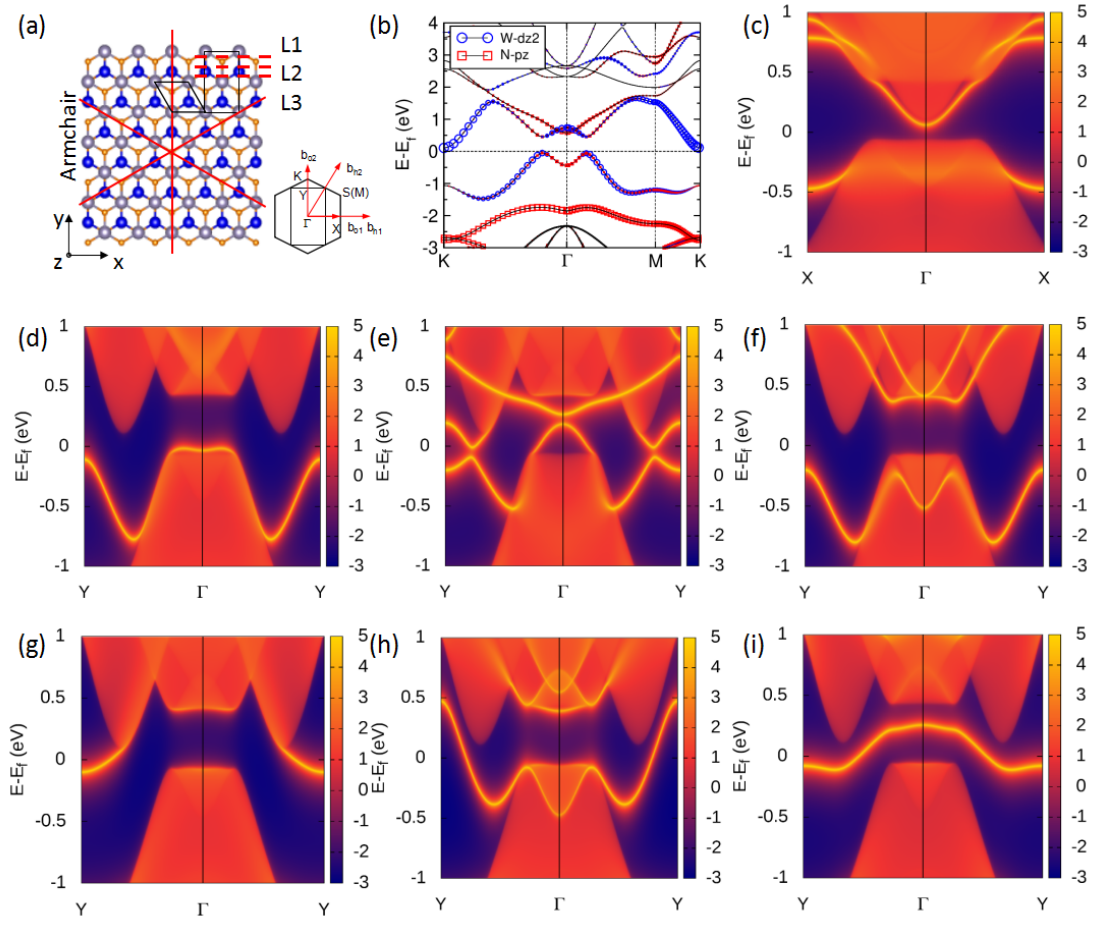


FIG. A1. (a) The top view of constructed orthorhombic cell of  $\alpha_2$ - $\text{WSn}_2\text{N}_4$ . The armchair edge is paralleled to mirror  $M_x$ .  $L_i^{up}$  and  $L_i^{down}$  ( $i=1, 2, 3$ ) are the edge above or below line  $L_i$ . The insert shows the Brillouin zone of orthorhombic and hexagonal cell. (b) The band structure of  $\alpha_2$ - $\text{WSn}_2\text{N}_4$ . The blue circles and red square are the weight of  $W_{dz^2}$  and  $N_{pz}$ . The spectral function for (c) armchair, (d)  $L1_{up}$ , (e)  $L1_{down}$ , (f)  $L2_{up}$ , (g)  $L2_{down}$ , (h)  $L3_{up}$  and (i)  $L3_{down}$  edges. The bright gold, red and navy part represent surface states, bulk states and vacuum, respectively.

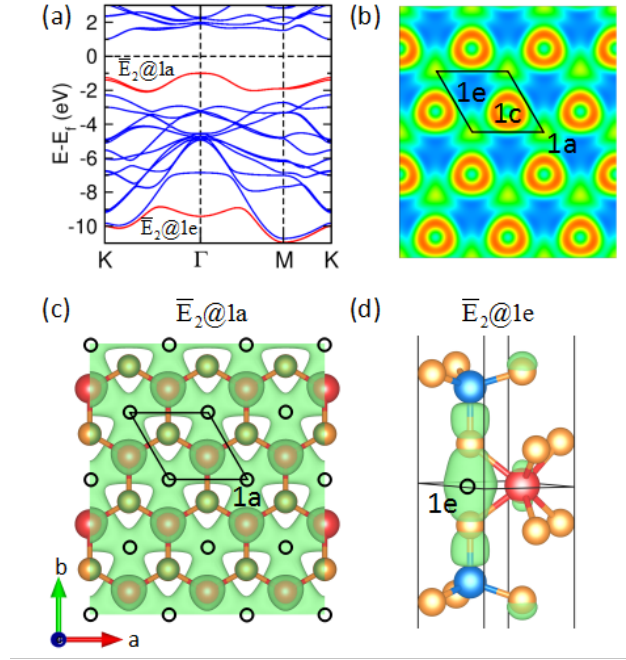


FIG. A2. Electronic structure of  $\alpha_2$ -MoSi<sub>2</sub>N<sub>4</sub> monolayer. (a) The band structure of  $\alpha_2$ -MoSi<sub>2</sub>N<sub>4</sub> monolayer, where the red bands correspond to the band representation of  $\bar{E}_2@1a$  and  $\bar{E}_2@1e$ . (b) The ELF of  $\alpha_2$ -MoSi<sub>2</sub>N<sub>4</sub> monolayer.  $1a$ ,  $1c$ , and  $1e$  are *Wyckoff* sites, and charges localize at *Wyckoff* sites  $1a$  and  $1c$ . The diamond solid line are the primitive cell of  $\alpha_2$ -MoSi<sub>2</sub>N<sub>4</sub> monolayer. The charges distribution of band representation  $\bar{E}_2@1a$  (c) and  $\bar{E}_2@1e$  (d) of  $\alpha_2$ -MoSi<sub>2</sub>N<sub>4</sub>. The green hook face is the isosurface with value of 0.008. The black circles are OWCCs at  $1a$  and  $1e$ .

TABLE A1. All possible decompositions of the BR of  $\alpha_1$ -MoSi<sub>2</sub>N<sub>4</sub> into linear combination of the EBRs in double space group  $P\bar{6}m2$  (No. 187). The first column gives the EBRs induced from different orbitals at *Wyckoff* positions  $1a$ ,  $1c$ , and  $1e$ ; the numbers below are the multiplicities of each EBR in the corresponding decomposition.

No.	$\bar{E}_1@1c$	$\bar{E}_2@1c$	$\bar{E}_3@1c$	$\bar{E}_1@1a$	$\bar{E}_2@1a$	$\bar{E}_3@1a$	$\bar{E}_1@1e$	$\bar{E}_2@1e$	$\bar{E}_3@1e$
#01	6	7	5	1	0	0	1	1	0
#02	5	6	4	2	1	1	1	1	0
#03	4	5	3	3	2	2	1	1	0
#04	3	4	2	4	3	3	1	1	0
#05	2	3	1	5	4	4	1	1	0
#06	1	2	0	6	5	5	1	1	0
#07	5	6	4	1	0	0	2	2	0
#08	4	5	3	2	1	1	2	2	1
#09	3	4	2	3	2	2	2	2	1
#10	2	3	1	4	3	3	2	2	1
#11	1	2	0	5	4	4	2	2	1
#12	4	5	3	1	0	0	3	3	2
#13	3	4	2	2	1	1	3	3	2
#14	2	3	1	3	2	2	3	3	2
#15	1	2	0	4	3	3	3	3	2
#16	3	4	2	1	0	0	4	4	3
#17	2	3	1	2	1	1	4	4	3
#18	1	2	0	3	2	2	4	4	3
#19	2	3	1	1	0	0	5	5	4
#20	1	2	0	2	1	1	5	5	4
#21	1	2	0	1	0	0	6	6	5



TABLE A2. All possible decompositions of the BR of  $\alpha_2$ - $\text{MoSi}_2\text{N}_4$  into linear combination of the EBRs in double space group  $\overline{\text{P}}\overline{6}\text{m}2$  (No. 187). The first column gives the EBRs induced from different orbitals at Wyckoff positions 1a, 1c, and 1e; the numbers below are the multiplicities of each EBR in the corresponding decomposition.

No.	$\overline{\text{E}}_1@1\text{c}$	$\overline{\text{E}}_2@1\text{c}$	$\overline{\text{E}}_3@1\text{c}$	$\overline{\text{E}}_1@1\text{a}$	$\overline{\text{E}}_2@1\text{a}$	$\overline{\text{E}}_3@1\text{a}$	$\overline{\text{E}}_1@1\text{e}$	$\overline{\text{E}}_2@1\text{e}$	$\overline{\text{E}}_3@1\text{e}$
#01	5	6	5	2	1	0	1	1	0
#02	4	5	4	3	2	1	1	1	0
#03	3	4	3	4	3	2	1	1	0
#04	2	3	2	5	4	3	1	1	0
#05	1	2	1	6	5	4	1	1	0
#06	0	1	0	7	6	5	1	1	0
#07	4	5	4	2	1	0	2	2	0
#08	3	4	3	3	2	1	2	2	1
#09	2	3	2	4	3	2	2	2	1
#10	1	2	1	5	4	3	2	2	1
#11	0	1	0	6	5	4	2	2	1
#12	3	4	3	2	1	0	3	3	2
#13	2	3	2	3	2	1	3	3	2
#14	1	2	1	4	3	2	3	3	2
#15	0	1	0	5	4	3	3	3	2
#16	2	3	2	2	1	0	4	4	3
#17	1	2	1	3	2	1	4	4	3
#18	0	1	0	4	3	2	4	4	3
#19	1	2	1	2	1	0	5	5	4
#20	0	1	0	3	2	1	5	5	4
#21	0	1	0	2	1	0	6	6	5

TABLE A3. Summary of OAI features of 17 34-VEC  $\text{MA}_2\text{Z}_4$  materials, 2H- $\text{MoS}_2$ , and  $\alpha$ -InSe .

No.	compounds name	phase type	OAI or not	OWCC
01	$\text{CrSi}_2\text{N}_4$	$\alpha_1$	Y	1a,1e
02	$\text{MoSi}_2\text{N}_4$	$\alpha_1$	Y	1a,1e
03	$\text{MoSi}_2\text{N}_4$	$\alpha_2$	Y	1a,1e
04	$\text{WSi}_2\text{N}_4$	$\alpha_1$	Y	1a,1e
05	$\text{MoGe}_2\text{N}_4$	$\alpha_1$	Y	1a
06	$\text{WGe}_2\text{N}_4$	$\alpha_1$	Y	1a
07	$\text{CrSi}_2\text{P}_4$	$\alpha_2$	Y	1a,1e
08	$\text{MoSi}_2\text{P}_4$	$\alpha_2$	Y	1a,1e
09	$\text{WSi}_2\text{P}_4$	$\alpha_2$	Y	1a,1e
10	$\text{CrGe}_2\text{P}_4$	$\alpha_2$	Y	1a
11	$\text{MoGe}_2\text{P}_4$	$\alpha_2$	Y	1a
12	$\text{WGe}_2\text{P}_4$	$\alpha_2$	Y	1a
13	$\text{MoSi}_2\text{As}_4$	$\alpha_2$	Y	1a,1e
14	$\text{WSi}_2\text{As}_4$	$\alpha_2$	Y	1a,1e
15	$\text{MoGe}_2\text{As}_4$	$\alpha_2$	Y	1a
16	$\text{WGe}_2\text{As}_4$	$\alpha_2$	Y	1a
17	$\text{WSn}_2\text{N}_4$	$\alpha_1$	Y	1a
18	$\text{MoS}_2$	2H	Y	1c,1e
19	InSe	$\alpha$	Y	1a,1c

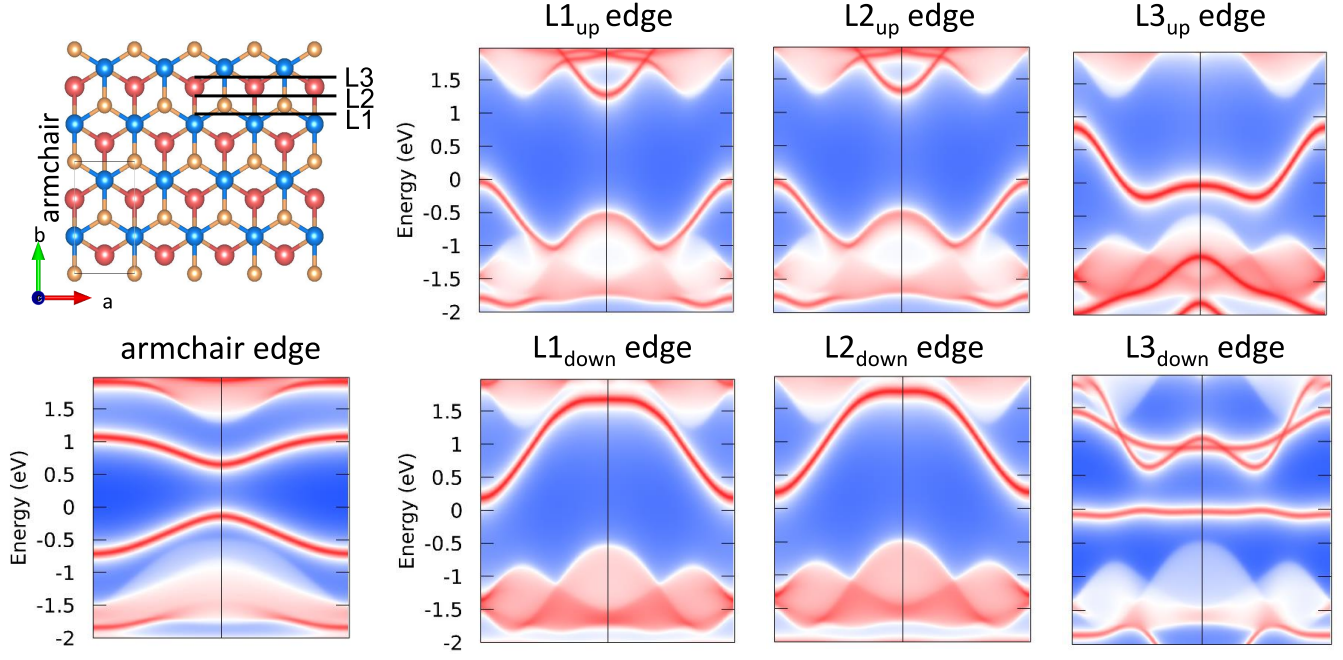


FIG. A3. (color online) The top left panel is the top view of MoSi<sub>2</sub>N<sub>4</sub> monolayer. There are seven types of edges. Armchair edge is clear shown in figure. Another six edges,  $L_{i_{up}}$  and  $L_{i_{down}}$  ( $i=1, 2, 3$ ) edge, are obtained by three cutting lines, where subscript up and down are the edge above or below line  $L_i$ . The projected edge states for  $L_{i_{up}}$  and  $L_{i_{down}}$  ( $i=1, 2, 3$ ) and armchair edges are shown in another six panels.

TABLE A4. The structural information about nine  $C_3$ -symmetric nanodisks, where center type "2N" means two N atoms at the center of nanodisk and "2Si 2N" means two N atom and two Si atoms at the center of nanodisk;  $N_{Mo}$ ,  $N_{Si}$ , and  $N_N$  are the number of atoms of Mo, Si, and N in nanodisk; SR is the stoichiometric ratio in nanodisk, normalized down to N atoms.

No.	$C_n$	shape	edge type	center type	$N_{Mo}$	$N_{Si}$	$N_N$	SR
01	$C_3$	hexagonal	armchair	2N	42	84	170	1.00:2.00:4.05
02	$C_3$	hexagonal	armchair	2Si 2N	42	86	170	1.00:2.05:4.05
03	$C_3$	hexagonal	armchair	1Mo	43	84	168	1.00:1.95:3.91
04	$C_3$	triangle	armchair	2N	30	60	122	1.00:2.00:4.07
05	$C_3$	triangle	armchair	2Si 2N	30	62	122	1.00:2.07:4.07
06	$C_3$	triangle	armchair	1Mo	31	60	120	1.00:1.94:3.87
07	$C_3$	triangle	$L2_{down}$	2N	15	42	98	1.00:2.80:6.53
08	$C_3$	triangle	$L1_{down}$	2Si 2N	21	56	86	1.00:2.67:4.10
09	$C_3$	triangle	$L3_{down}$	1Mo	28	30	72	1.00:1.07:2.57

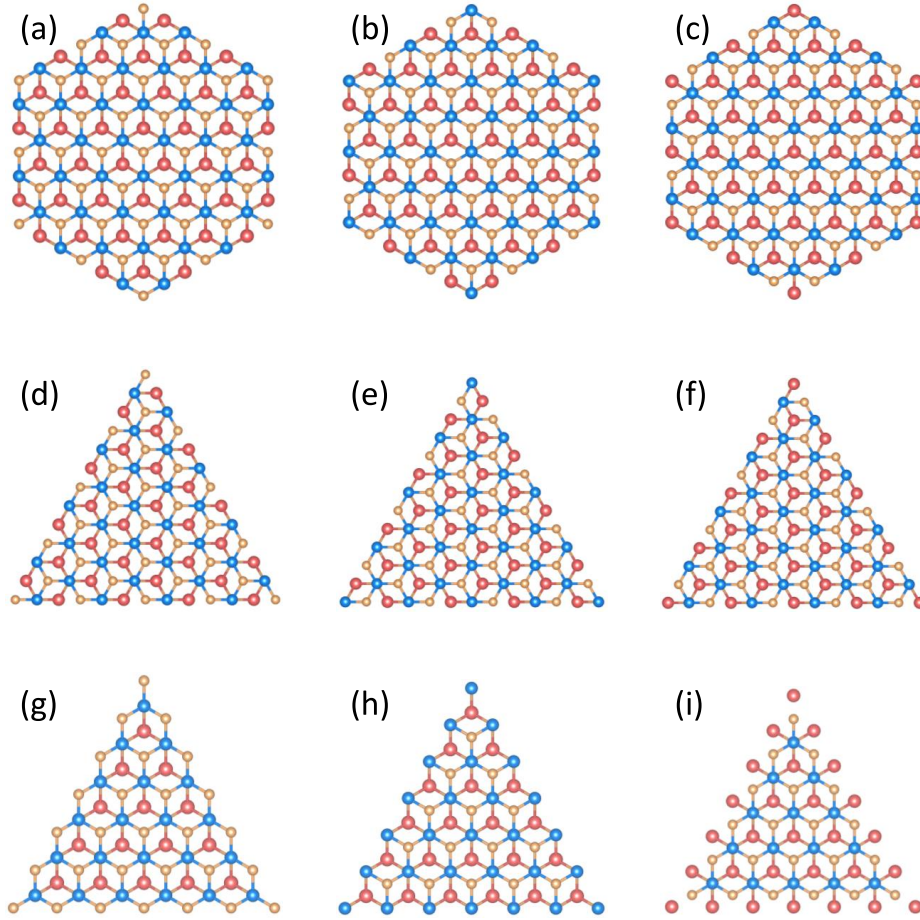


FIG. A4. (color online) Hexagonal and triangle  $C_3$ -symmetric nanodisk with armchair, and  $L_{i_{down}}$  ( $i = 1, 2, 3$ ) edge, corresponding to **Table A4**.

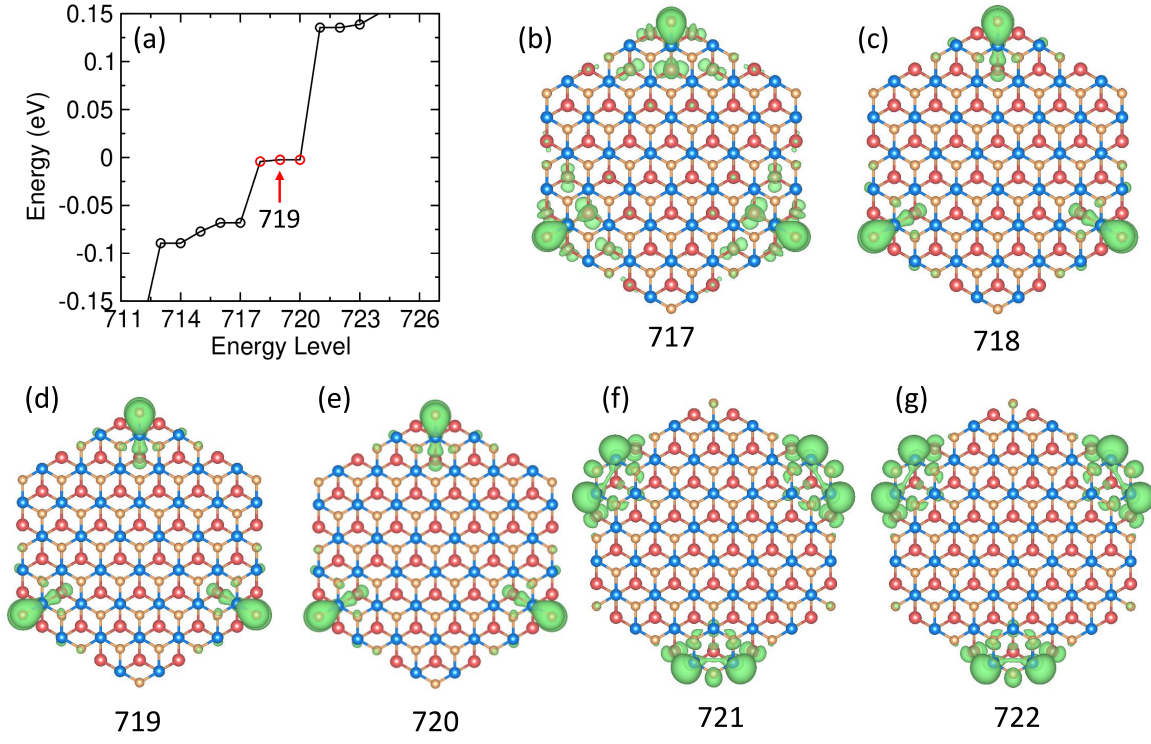


FIG. A5. (color online) (a) The energy spectrum of  $C_3$ -symmetric N-centered hexagonal nanodisk of  $\text{MoSi}_2\text{N}_4$ . Where red circles is corner states. (b-g) show the charge distribution of its corresponding energy level.

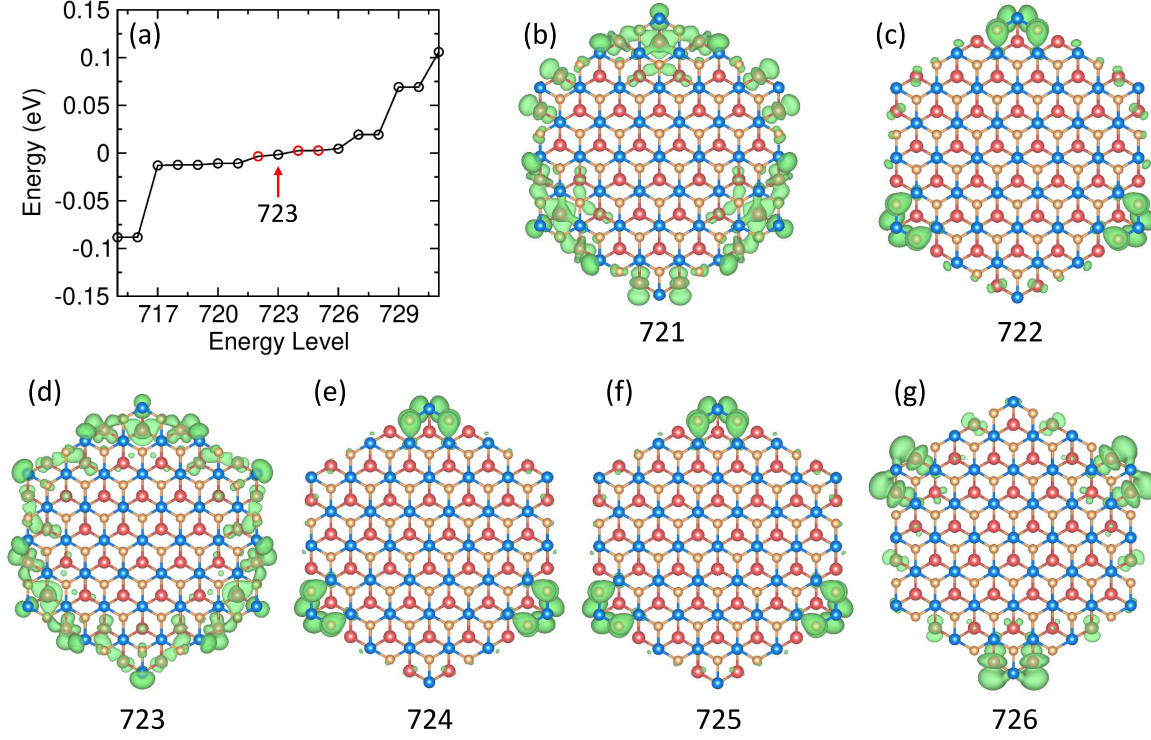


FIG. A6. (color online) (a) The energy spectrum of  $C_3$ -symmetric Si-centered hexagonal nanodisk of  $\text{MoSi}_2\text{N}_4$ . Where red circles is corner states. (b-g) show the charge distribution of its corresponding energy level.



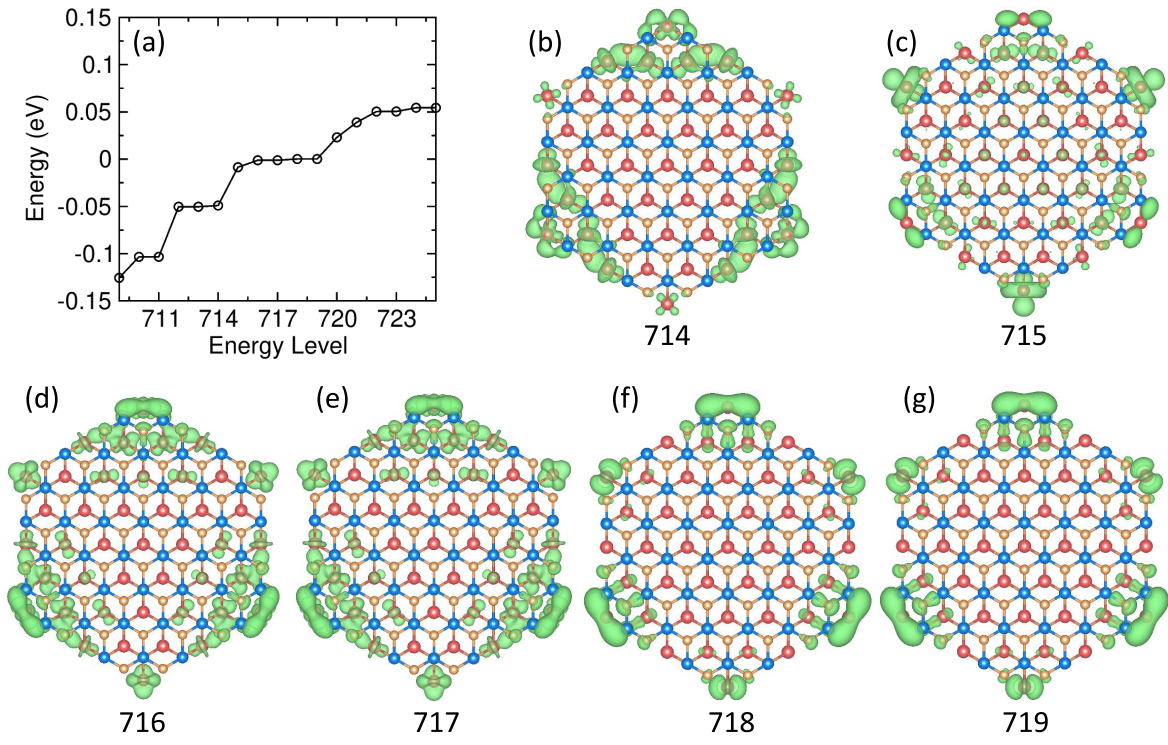


FIG. A7. (color online) (a) The energy spectrum of  $C_3$ -symmetric Mo-centered hexagonal nanodisk of  $\text{MoSi}_2\text{N}_4$ . (b-g) show the charge distribution of its corresponding energy level.